

# Microstructural Evolution and Strain-Compensated Constitutive Equation for As-Cast Mg-3Sn-1Mn-1La Alloy During Isothermal Compression

Zhang Libin<sup>1,3</sup>, Liu Guangming<sup>1,3</sup>, Han Tingzhuang<sup>1,3</sup>, Huang Wenzhan<sup>1</sup>, Wang Rongjun<sup>2,3</sup>, Ma Lifeng<sup>2,3</sup>

<sup>1</sup> School of Materials Science and Engineering, Taiyuan University of Science and Technology, Taiyuan 030024, China; <sup>2</sup> School of Mechanical Engineering, Taiyuan University of Science and Technology, Taiyuan 030024, China; <sup>3</sup> Coordinative Innovation Center of Taiyuan Heavy Machinery Equipment, Taiyuan University of Science and Technology, Taiyuan 030024, China

**Abstract:** Hot deformation behavior and microstructural evolution of the as-cast Mg-3Sn-1Mn-1La alloy were investigated by isothermal compression at temperature of 200~450 °C and strain rate of 0.001~1.0 s<sup>-1</sup>. The results show that the flow stress increases obviously with the decrease of the temperature and the increase of the strain rate. The recrystallized grain size increases with increasing the temperature and decreasing the strain rate. At lower deformation temperatures, many twins form to coordinate deformation and continuous dynamic recrystallization is the main mechanism. However, discontinuous dynamic recrystallization becomes the predominant operating mechanism of dynamic recrystallization at high deformation temperature. Plate-shaped MgSnLa compounds, which have a coherent relationship with the matrix, have a pinning effect on the  $\alpha$ -Mg grain boundary. The effects of friction and deformation heating on flow stress were analyzed and corrected. The results show that deformation heating has a significant influence on the flow stress at higher strain rates and lower temperatures, while the influence of frictional effect is slight. Based on the experimental results, a strain-compensated Arrhenius-type equation was developed. Comparison of the experimental data with the calculated flow stress indicates that the developed constitutive equations can adequately describe the hot deformation behavior of the experimental alloy.

**Key words:** Mg-Sn based alloy; hot deformation; constitutive equation; dynamic recrystallization

Magnesium alloys have been used in aircraft and automobile industries due to its corresponding advantages, such as high specific strength and low density<sup>[1]</sup>. However, the restricted heat resistance, ductility and formability strongly hinder the wide applications of magnesium alloys<sup>[2]</sup>. In recent years, the Mg-Sn based alloys have aroused many concerns<sup>[3-6]</sup>. Owing to the formation of thermal-stable Mg<sub>2</sub>Sn phases with high melting temperature (higher than the melting temperature of Mg<sub>17</sub>Al<sub>12</sub>), the Mg-Sn-based alloys show promising mechanical properties of Mg alloys at room temperature and high temperature<sup>[7]</sup>. The melting

temperature of Mg<sub>2</sub>Sn is 778 °C<sup>[8]</sup>, and Mg-Sn-based alloys exhibit higher creep properties at 150 °C<sup>[9]</sup>. The addition of Mn element in Mg alloys can improve the corrosion resistance and refine the grain size<sup>[5,10,11]</sup>. The addition of rare earth (RE) elements can also improve the mechanical performance of the Mg-Sn alloys. For instance, Wei et al<sup>[12]</sup> investigated the influence of La addition on creep properties of Mg-Sn-La alloys and found that Mg-Sn-La alloy exhibits superior creep properties than Mg-Sn alloy does. Zhao et al<sup>[13]</sup> studied the effect of La on the microstructure and mechanical properties of Mg-3Sn-1Mn-xLa alloy and

Received date: March 22, 2020

Foundation item: Natural Science Foundation of Shanxi Province (201901D111241); Key Research and Development Program of Shanxi Province (201603D111004, 201703D111003); Major Science and Technology Projects of Shanxi Province (20181101002); National Natural Science Foundation of China (U1610253, U610256, 51604181)

Corresponding author: Liu Guangming, Ph. D., Professor, School of Materials Science and Engineering, Taiyuan University of Science and Technology, Taiyuan 030024, P. R. China, E-mail: liugm@tyust.edu.cn

Copyright © 2021, Northwest Institute for Nonferrous Metal Research. Published by Science Press. All rights reserved.

found that the maximum tensile strength and elongation are obtained with 1.0wt% La. The above studies of Mg-Sn-based alloys mainly focused on the alloying element addition. While hot working is a typical and widely used metal formation method which can also improve the mechanical properties of materials<sup>[14]</sup>. Therefore, it is necessary to investigate the effects of deformation conditions on the microstructure evolution and the flow behavior during hot working process of the Mg-Sn-Mn-La alloy.

A reliable constitutive model is very important for describing the plastic flow behaviors in deformation processes, such as rolling and forging. The constitutive models can usually be divided into three categories: physical based models, artificial neural network (ANN) and phenomenological models<sup>[15]</sup>. Compared with physical based models, the phenomenological models involve less material constants and the required experiments can be easily conducted<sup>[16]</sup>. Therefore, various phenomenological models, such as Johnson-Cook (JC) models and Arrhenius models, are used for the flow stress prediction. Many Arrhenius models with and without strain compensation have been established because they can accurately describe the relationship between flow stress, temperature and strain rate<sup>[8,17,18]</sup>.

In order to build a reliable constitutive model, the accuracy of flow stress data is also important. Although various lubricants are used to reduce the effect of friction during testing, the cylindrical specimen still becomes barrel-shaped after compression instead of a standard cylindrical shape, which indicates that the friction effect is eliminated completely. Errors still exist in experimental data because friction leads to an increase in the as-measured flow stress. Besides, when specimen is subjected to the large plastic deformation during experiment, a significant proportion of the plastic work converts into deformation heating, which may cause an obvious increase in sample temperature<sup>[19]</sup>. In that case, the actual flow stress is higher than the experimental flow stress. In order to improve the accuracy of constitutive equation, friction correction and deformation heating correction are essential.

In this research, the hot deformation behavior of Mg-3Sn-1Mn-1La alloy was studied by hot compression test at temperature of 200~450 °C and strain rate of 0.001~1 s<sup>-1</sup>. The effects of temperature and strain rate on the microstructure and dynamic recrystallization (DRX) behavior of this alloy were investigated by optical microscope (OM), transmission electron microscope (TEM) and electron backscatter diffraction (EBSD) techniques. A constitutive equation was proposed based on an Arrhenius equation, and the Zener-Hollomon parameters, considering the effects of friction, deformation heating and strain, were used to model the flow behavior of Mg-3Sn-1Mn-1La alloy. The reliability of the constitutive equation was evaluated.

## 1 Experiment

Alloy ingots of Mg-3Sn-1Mn-1La alloys were prepared by induction melting in an electric resistance furnace under the mixed protective gases of CO<sub>2</sub> and SF<sub>6</sub>. The chemical composition of Mg-3Sn-1Mn-1La used in the present study is given in Table 1.

After casting, the ingot was homogenized at 380 °C for 8 h followed by air cooling to reduce the non-homogeneity in composition and microstructure. The microstructure of Mg-3Sn-1Mn-1La alloy after homogenization is shown in Fig.1a. The initial grains of the alloy are equiaxed and large with an average size of ~70 μm. As shown in Fig.1, the second phase with continuous net structure mainly is distributed at the grain boundaries. Based on EDS analysis and XRD results (Fig.1b and Fig.2, respectively), the compounds formed at the grain boundaries are MgSnLa compounds composed of Mg<sub>2</sub>Sn, Mg<sub>17</sub>La<sub>2</sub> and La<sub>5</sub>Sn<sub>3</sub> phases.

Cylindrical shaped specimens with the dimension of Φ10 mm×15 mm were prepared for isothermal compression tests. The hot compression tests were conducted on the Gleeble-3800 thermo-mechanical simulator at deformation temperatures of 200~450 °C (interval of 50 °C) and strain rates of 0.001, 0.01, 0.1, and 1.0 s<sup>-1</sup>. To obtain uniform temperature, specimens were heated to corresponding test tempera

Table 1 Chemical composition of experimental alloy (wt%)

Sn	Mn	La	Si	Cu	Ni	Fe	Mg
3.09	0.98	1.07	0.045	0.0026	0.0031	0.0034	Bal.

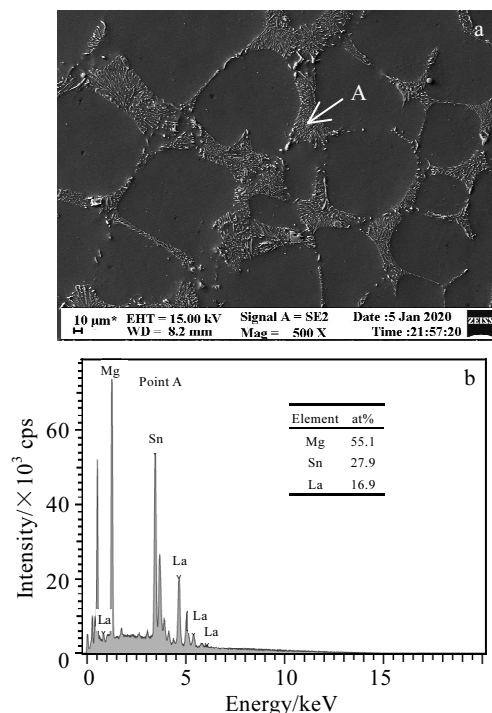


Fig.1 SEM image (a) and EDS analysis (b) of Mg-3Sn-1Mn-1La alloy

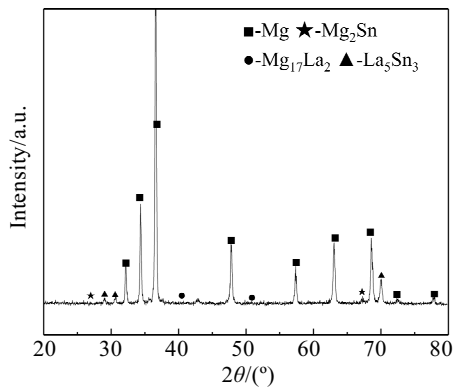


Fig.2 XRD pattern of homogenized Mg-3Sn-1Mn-1La alloy

tures with the rising rate of 5 °C/s and consequently kept for 90 s. All specimens were compressed to the state of total true strain of 0.7. To study the effect of strain on microstructure evolution, some additional specimens were compressed at 400 °C and 0.1 s<sup>-1</sup> to the state of true strain of 0.2 and 0.4 separately. After compression, the compressed specimens were immediately water-cooled to maintain the microstructure.

The hot deformed specimens were sectioned parallel to the compression axis. The specimen surfaces were ground with gradually finer SiC papers (800#~2000#) and polished mechanically. After polishing, the specimens were etched by a solution of 4.2 g picric acid, 8 mL acetic acid, 5 mL water and 50 mL ethanol. The phase identification of the surface was performed by X-ray diffraction (XRD, X'Pert). The microstructures at the center of the cross-sectional surface were characterized by scanning electron microscope (SEM, ZEISS Aztec INCA) equipped with energy dispersive spectroscopy (EDS), EBSD and TEM (JEM-F200). The EBSD investigation was performed on a Nordlys Nano from OXFORD, and the step size was 0.5 μm. The corresponding data were analyzed by the HKL's channel 5 software.

## 2 Results and Discussion

### 2.1 True stress-strain curves

Fig.3 shows the true stress-strain curves at various strain rates and temperatures. It can be observed from Fig.3a that the flow stress increases with the increase of the strain rate. The peak stress of the alloy increases from 59 MPa to 98 MPa when strain rates increase from 0.001 to 1 s<sup>-1</sup>. This is because there is not enough time for dislocation rearrangement and annihilation at higher strain rate, which leads to the work hardening effect. It can also be observed from Fig.3b that the peak stress of the alloy decreases from 109 MPa to 27 MPa when temperature increases from 200 to 450 °C. With the increase of temperature, the critical shear

stress of crystal slip decreases, which reduces the obstacle of dislocation motion<sup>[20]</sup>. Moreover, dynamic recovery (DRV) and dynamic recrystallization are more likely to occur at higher temperature, resulting in the decrease of dislocation density<sup>[21]</sup>. Therefore, the flow stress decreases.

In general, all curves exhibit similar trends which can be divided into hardening and softening stages. The work hardening rate, which can be obtained by equation  $\theta = d\sigma/d\varepsilon$ <sup>[22]</sup> through true stress-strain curves, is usually used to describe the hot deformation behavior of metals. Fig.4 shows the relationship of the sample compressed at 400 °C and 0.1 s<sup>-1</sup>. At the beginning of work hardening stage, the strain hardening rate is relatively high and the dislocations accumulate continually with the increase of the strain, which makes the flow stress increase rapidly. As the strain increases, the work hardening rate decreases, which means that the dynamic softening including DRV and DRX occurs.

However, the dynamic softening effect is weaker than that of work hardening and the flow stress keeps increasing. After reaching the peak stress value, the flow stress decreases gradually and the deformation enters the softening stage. It is known that the deformation usually enters a steady stage, where work hardening and softening effects reach the dynamic balance and  $\theta$  maintains nearby zero. However, the flow stress continues to decline and the value of  $\theta$  maintains negative even at the end of the curve with the strain of 0.7, which indicates that the dynamic softening still predominates till the end of the hot deformation process.

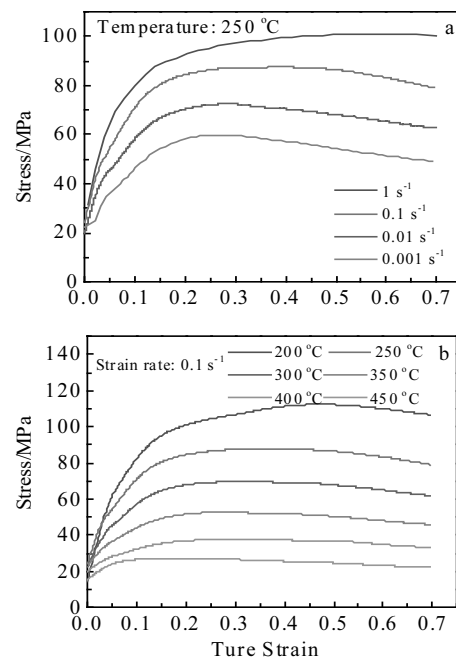


Fig.3 True strain-stress curves under different conditions: (a)  $T=250\text{ }^{\circ}\text{C}$  and (b)  $\dot{\varepsilon}=0.1\text{ s}^{-1}$

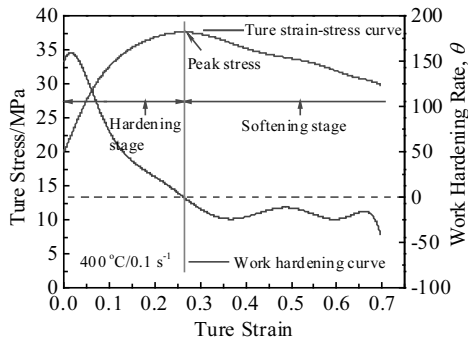


Fig.4 True stress-strain and work hardening rate,  $\theta$ -strain curves

**2.2 Microstructural evolution**

In order to study the microstructure characteristics at each deformation stage, some specimens were examined by TEM. Fig.5 shows TEM images of samples compressed at 400 °C/0.1 s<sup>-1</sup> with strains of 0.2, 0.4 and 0.7. Fig.5a indicates that the original grains elongate along the compression direction with high dislocation density, and cell structure produced by dislocation tangle is the main microstructural feature at the strain of 0.2. At the strain of 0.4, dislocation walls build at subgrain boundaries due to the dislocation motion and rearrangement, as shown in Fig.5b. Fig.5c shows DRX grains with regular and clear grain boundaries, which are the evidence of recrystallization. The characterization of TEM microstructures at different strains accounts for the variation of flow stress. The flow stress increases rapidly to a peak value due to work hardening with the formation of tangled dislocations. Then the stress decreases gradually, which results from dynamic softening caused by DRV and DRX<sup>[23]</sup>. Then the specimens remain in a stable state, which is the result of the cooperation of work hardening and dynamic softening effects during hot deformation.

Fig.6 presents the inverse pole figures (IPFs) of the deformed specimens with true strain of 0.7 at various temperatures and strain rates observed by EBSD. The coarse original grains elongate along the compression direction

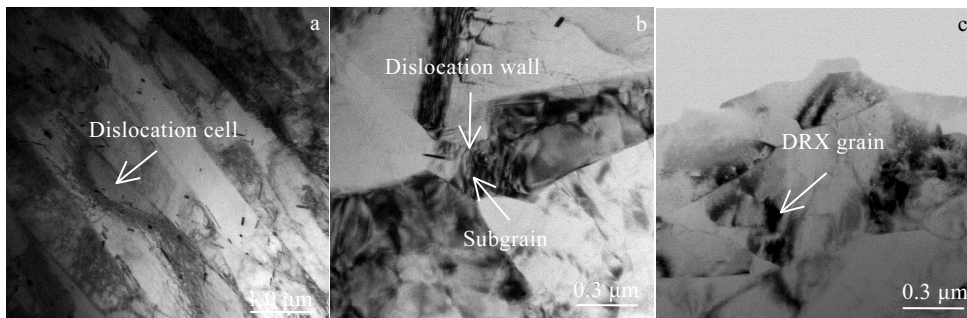


Fig.5 TEM images of specimens deformed at 400 °C/0.1 s<sup>-1</sup> with different strains: (a)  $\epsilon=0.2$ , (b)  $\epsilon=0.4$ , and (c)  $\epsilon=0.7$

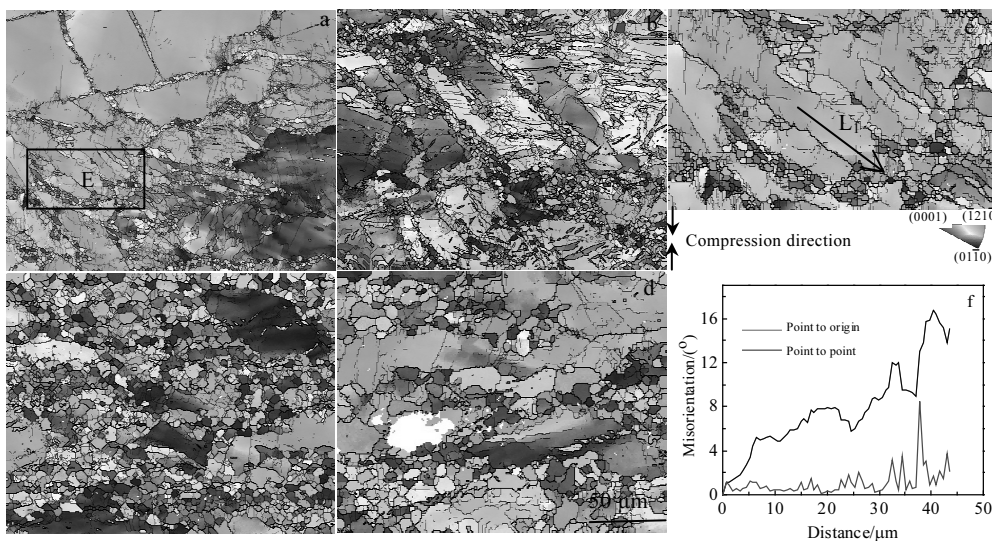


Fig.6 Inverse pole figures (IPFs) of specimens deformed under different conditions: (a) 200 °C/0.1 s<sup>-1</sup>; (b) 300 °C/0.1 s<sup>-1</sup>; (c) 400 °C/0.1 s<sup>-1</sup>; (d) 400 °C/0.01 s<sup>-1</sup>; (e) enlarged IPF map of region marked E in Fig.6a; (f) cumulative misorientation profile along L1 direction in Fig.6e

and many new DRX grains form. At 200~300 °C/0.1 s<sup>-1</sup>, some DRX grains are observed at the intersection of twins and grain boundaries, as shown in Fig.6a and 6b. With the temperature increasing to 400 °C, many grain boundaries become serrated and bulged, and the original coarse grains are partially replaced by DRX grains, as shown in Fig.6c. The fraction and average size of DRX grains increase with increasing the temperature from 200 °C to 400 °C, comparing the microstructures in Fig.6a~6c<sup>[24]</sup>. Furthermore, with the decrease of strain rate from 0.1 to 0.01 s<sup>-1</sup> at 400 °C, DRX grain size increases (Fig.6d) and DRX proceeds more thoroughly because of the more deformation time for the nucleating and growing of DRX grains<sup>[25]</sup>. Meanwhile, there are still many elongated original grains, indicating that the DRX process is incompletely.

In Fig.6a and 6b, a lot of twins form in the original coarse grains, and fine DRX grains are observed near the coarse grain boundaries. Under the high strain rate and low temperature conditions, due to the restricted slip systems of close-packed hexagonal (hcp) structure, DRX process is restricted, and many twins form to coordinate deformation. It can be seen from the Fig.7a that the original grains are separated into many twins and twin boundaries hinder the movement of dislocations. Therefore, many dislocations accumulate around the twin boundaries. The local misorientation is imaged by Kernel Average Misorientation (KAM) mapping, as shown in Fig.7b, and used as a measurement of the intragranular misorientation of the specimen. KAM value is related to the dislocation density. It can be observed that the new recrystallized grains with lower dislocation density (blue color in Fig.7b) at the twin boundaries exist in the initial grains. Meanwhile, the new grains nucleate as a consequence of formation of twin segment along the boundary of the deformed grain, implying that the formation of nucleus at the twin boundaries can serve as a supplementary mechanism for the nucleation of DRX<sup>[26]</sup>. Fig.7b also shows the relatively high values of dislocation density. The dislocations are mainly distributed at the grain boundaries and twin boundaries, which supports that the grain boundaries and twin boundaries effectively pin the dislocations and the microstructural evolutions are not yet accompanied. DRX grains in twins formed during the process at the low-angle grain boundaries in twins grow to high-angle grain boundaries with the increase of the strain, which is a typical character for the continuous dynamic recrystallization (CDRX). With the increase of deformation temperature, the critical shear stress of twins decreases, which decreases the stress concentration to hinder the twin nucleation. Meanwhile, the cross-slip and non-basal slip are activated at higher deformation temperatures, and DRX occurs easily at the original grain boundaries.

In order to illustrate the DRX mechanism, the corresponding grain boundary angles are measured, as shown in

Fig.8. Low angle grain boundary (LAGB, 2°~15°) and high angle grain boundary (HAGB, >15°) are in red and black, respectively. Fig.8e exhibits the misorientation angle distribution under different conditions, and it is clear that as the deformation temperature increases and the strain rate decreases, the fraction of HAGB increases due to the formation of recrystallized grains. As shown in Fig.8a and 8b, the grain boundaries are relatively flat, many twins form in the original coarse grains under the lower deformation temperature, and a lot of new small recrystallized grains form along the original grain boundaries forming a necklace type structure. In addition, the point to origin misorientation and point to point misorientation along the labeled line (L<sub>1</sub> in Fig.6e) are obtained based on the orientation analysis. Fig.6e shows the cumulative misorientation profile of parent grains from the center to the grain boundary, and a significant increase in the misorientation along the line is observed. The above analyses indicate that the main mechanism of DRX under lower deformation temperature is CDRX mechanism<sup>[27]</sup>. The generation and tangle of dislocations produce many subgrain structures in the initial grains at the early stage of deformation. As the deformation progresses, these LAGBs become HAGBs through constantly absorbing dislocations, thereby leading to the formation of equiaxed DRX grains<sup>[28]</sup>. However, when the deformation temperature increases and strain rate decreases,

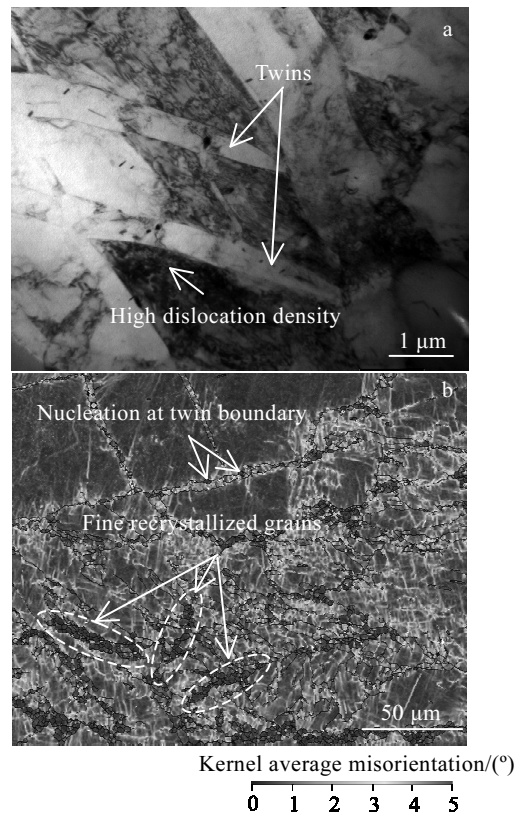


Fig.7 TEM image (a) and KAM map (b) of specimen deformed at 200 °C/0.1 s<sup>-1</sup>

as shown in Fig.8c and 8d, the initial grain boundaries bulge and a lot of recrystallization nuclei form along the initial grain boundaries, suggesting the occurrence of discontinuous dynamic recrystallization (DDRX) during hot deformation<sup>[29]</sup>. As the temperature increases, the grain boundaries migration rate increases obviously, and the inhibition effect of the grain boundary on the motion of dislocations reduces, making the formation of pile-up dislocations difficult and also decreasing the stress concentration to hinder the twin nucleation<sup>[30]</sup>. As a result, the CDRX process is hindered under such conditions. Based on the

above analysis, DDRX mechanism is the main DRX mechanism under high deformation temperature and low strain rate.

Fig.9 presents the OM image and TEM images of the deformed specimens with true strain of 0.7 at 400 °C/0.1 s<sup>-1</sup>. It can be seen from Fig.9a that some fine DRX grains form near the particles, which are large enough to encourage the particle stimulate nucleation (PSN) mechanism<sup>[31]</sup>. PSN usually occurs around particles with a diameter greater than ~1 μm. As shown in Fig.9b, it contains two typical types of precipitates: plate-shaped precipitates with the average

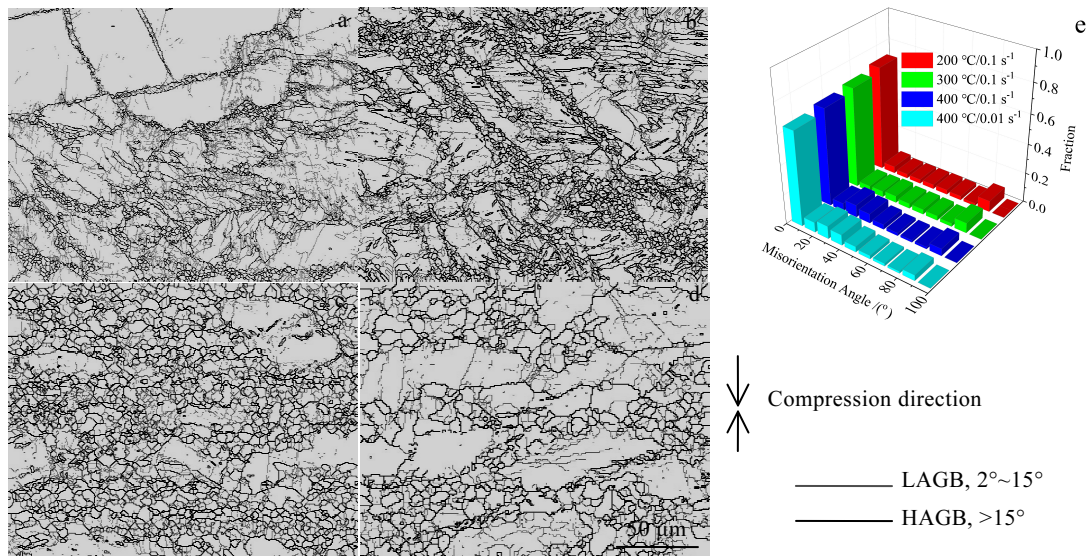


Fig.8 Grain boundary maps of samples deformed under different conditions: (a) 200 °C/0.1 s<sup>-1</sup>; (b) 300 °C/0.1 s<sup>-1</sup>; (c) 400 °C/0.1 s<sup>-1</sup>; (d) 400 °C/0.01 s<sup>-1</sup>; (e) misorientation angle distribution

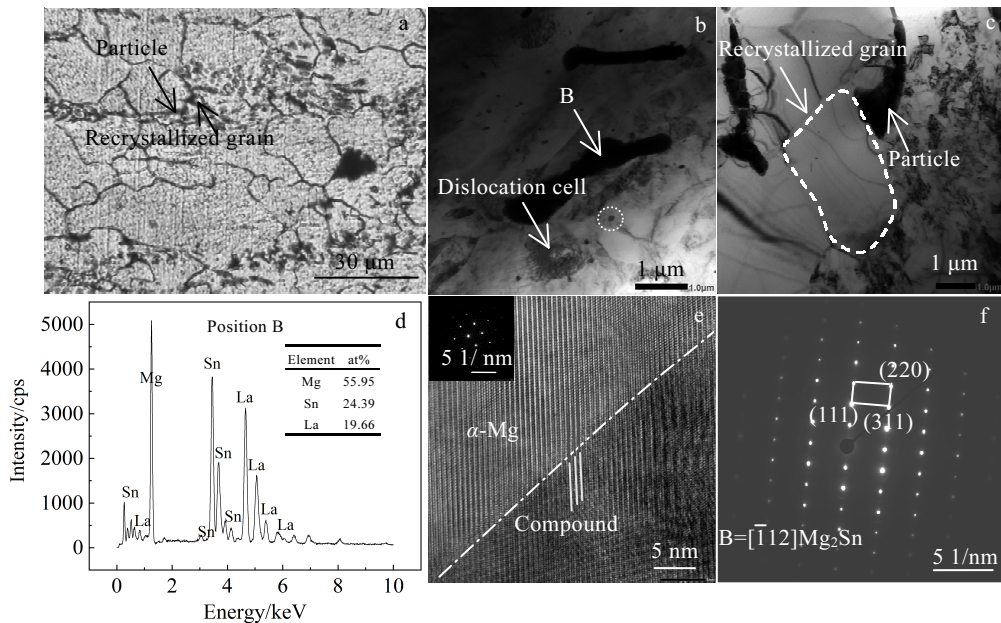


Fig.9 Microstructures analyses of deformed specimens with true strain of 0.7 at 400 °C/0.1 s<sup>-1</sup>: (a) OM image; (b) bright field TEM image; (c) microstructure near the broken particles; (d) EDS analysis of position B in Fig.9b; (e) high-resolution TEM image of MgSnLa compounds; (f) SAED pattern of the white circle region in Fig.9b

length of 2  $\mu\text{m}$  and the average width of 250 nm; spheroidized precipitates with the average diameter of 80 nm. The plate-shaped precipitates, which are identified as MgSnLa compounds from the EDS results (Fig.9d), are mainly distributed at the grain boundaries. As shown in Fig.9e, the MgSnLa compounds are coherent with the  $\alpha$ -Mg matrix. During the deformation, the MgSnLa compounds effectively pin the movement of dislocation and grain boundaries, inhibiting the microcracks and enhancing the mechanical properties of the alloy. As shown in Fig.9b and 9c, a lot of dislocations move and gather near the MgSnLa compounds, resulting in the formation of DRX grains. Moreover, as the white circle region in Fig.9b shows, many fine spherical precipitates are detected, and the selected area electron diffraction (SAED) results (Fig.9f) indicate that this spheroidized precipitate is Mg<sub>2</sub>Sn phase. Because of the relatively high melting temperature (778 °C), the Mg<sub>2</sub>Sn phase can effectively pin the dislocation movement at room temperature and high temperature and improve the mechanical properties of the alloy.

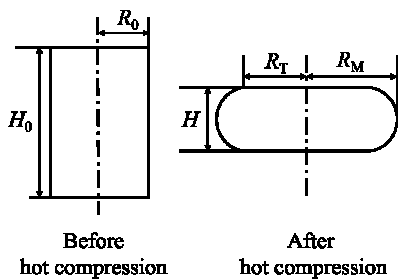
### 2.3 Correction of true strain-stress curves

#### 2.3.1 Deformation friction correction

Fig.10 shows the schematic diagram of isothermal compression test sample.

In this study, isothermal compression experimental data are evaluated by the physical quantity of expansion coefficient  $B$  proposed by Roebuck<sup>[24]</sup>. When  $B < 1.1$ , it can be considered that the friction effect in compression experiment is small and no correction is needed. When  $B \geq 1.1$ , the friction effect has great influence on the experimental data, and necessary corrections should be made<sup>[19]</sup>. The  $B$  parameter is calculated by Eq.(1) and the meaning of related parameters is the same with that in Fig.10:

$$B = \frac{HR_M^2}{H_0R_0^2} \quad (1)$$



$H$ -height of the compressed sample;  $R_M$ -maximum radius after deformation of sample;  $R_T$ -top radius of cylinder after deformation;  $H_0$ -height of the original sample;  $R_0$ -radius of the original sample

Fig.10 Schematic diagram of isothermal compression test sample

As shown in Fig.11, all the values of  $B$  under the deformation conditions of this study exceed 1.1, so it is necessary to consider the friction correction.

The results of Ebrahimi's research<sup>[32]</sup> indicate that the coefficient of friction  $\mu$  between the sample and indenter during the isothermal compression deformation can be calculated by Eq.(2):

$$\mu = \frac{\left(\frac{R}{H}\right)b}{\left(\frac{4}{\sqrt{3}}\right) - \left(\frac{2b}{3\sqrt{3}}\right)} \quad (2)$$

with

$$b = 4 \frac{\Delta R}{R} \frac{H}{\Delta H}$$

$$R_T = \sqrt{3 \frac{H_0}{H} R_0^2 - 2 R_M^2}$$

where  $b$  is the barrel parameter;  $\Delta R$  is the difference between maximum and top radius ( $\Delta R = R_M - R_T$ );  $R$  is the average radius of cylinder after deformation ( $R = R_0 \sqrt{H_0/H}$ );  $\Delta H$  is the height reduction ( $\Delta H = H_0 - H$ ).

The flow stress can be corrected by Eq.(3):

$$\sigma^f = k\sigma \quad (3)$$

with

$$k = \frac{C^2}{2[\exp(C) - C - 1]}$$

$$C = \frac{2\mu R_0}{H_0}$$

where  $\sigma^f$  is the flow stress after friction correction,  $\sigma$  is the experimentally measured flow stress, and  $k$  is the friction correction coefficient.

Fig.12a and 12b show the comparison of the true stress-strain curves before and after friction correction at 250 °C and strain rate of 0.1 s<sup>-1</sup>, respectively. It can be observed that the frictional effect has a greater impact at high strain rates and low temperatures. At 200 °C/1 s<sup>-1</sup>,

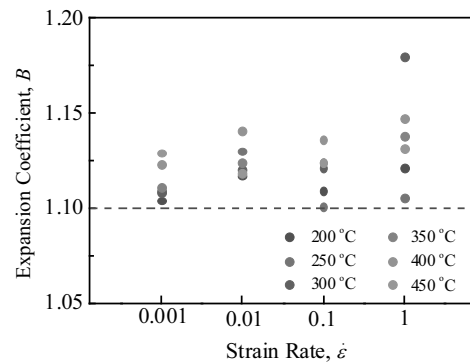


Fig.11 Values of  $B$  under different deformation conditions

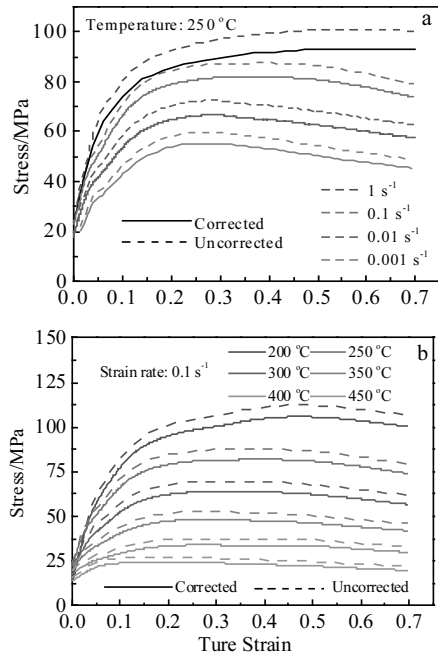


Fig.12 Comparison of true stress-strain curves before and after friction correction under different conditions: (a)  $T=250\text{ }^{\circ}\text{C}$  and (b)  $\dot{\varepsilon}=0.1\text{ s}^{-1}$

the maximum friction correction is 14 MPa.

### 2.3.2 Deformation heating correction

Due to the deformation heating effect, the temperature increases significantly depending on the materials and deformation conditions, such as strain, deformation temperature and strain rate. The temperature rise ( $\Delta T$ ) can be described as Eq.(4)<sup>[33]</sup>:

$$\Delta T = \frac{0.95\eta}{\rho C_p} \int_0^{\varepsilon} \sigma d\varepsilon \quad (4)$$

where  $C_p$  is the specific heat,  $\rho$  is the material density,  $\varepsilon$  is the strain,  $\sigma$  is the flow stress, and  $\eta$  is the thermal efficiency, calculated by Eq.(5).

$$\eta = \begin{cases} 0 & \dot{\varepsilon} \leq 10^{-3} \text{ s}^{-1} \\ (0.316)\lg \dot{\varepsilon} + 0.95 & 10^{-3} \text{ s}^{-1} < \dot{\varepsilon} < 1.0 \text{ s}^{-1} \\ 0.95 & \dot{\varepsilon} \geq 1.0 \text{ s}^{-1} \end{cases} \quad (5)$$

Values of  $\Delta T$  are calculated via Eq.(4) and Eq.(5) for strains in the range of 0.1~0.7 with an interval of 0.2. Fig.13a shows the variation of  $\Delta T$  with  $\varepsilon$  for samples deformed at different strain rates and deformation temperatures. It can be observed that  $\Delta T$  increases with the increase of  $\varepsilon$ , due to the accumulation of the deformation heat. Fig.13b shows the detailed variation at different strain rates and deformation temperatures with the strain of 0.7. It can be observed that  $\Delta T$  decreases with the increase of temperature and the decrease of strain rate.

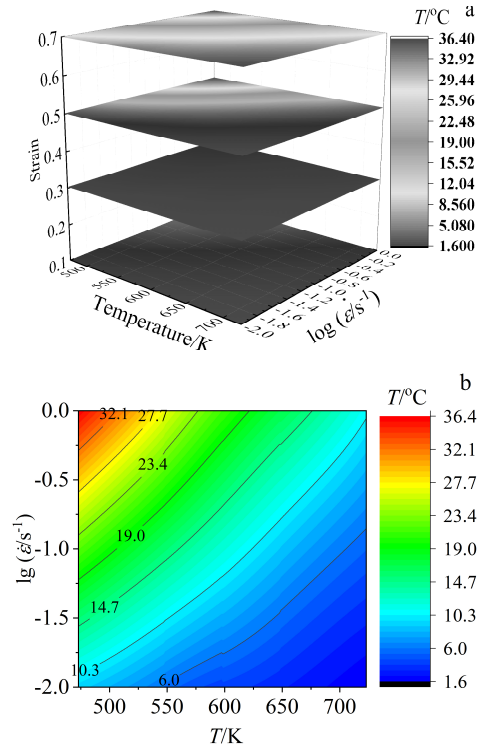


Fig.13 Temperature variation under different deformation conditions: (a) at true strain from 0.1 to 0.7 and (b) at the strain of 0.7

Moreover, it is obvious that  $\Delta T$  is more pronounced at higher strain rates and lower deformation temperatures. With the increase of  $\dot{\varepsilon}$ , there is little time for deformation heat to dissipate which results in the larger  $\Delta T$ <sup>[19]</sup>. The temperature rise has a great impact on the flow stress, and the flow stress value need to be corrected for a reliable constitutive equation.

The isothermal flow stress  $\sigma^l$  can be determined by Eq.(6):

$$\sigma^l(\varepsilon, \dot{\varepsilon}, T_0) = \sigma^H(\varepsilon, \dot{\varepsilon}, T_0) - \frac{\partial \sigma^l(T_i)}{\partial T_i} \Big|_{\varepsilon, \dot{\varepsilon}} \Delta T \quad (6)$$

where  $\sigma^l$  is the corrected stress, and  $\sigma^H$  is uncorrected flow stress. In this study,  $\sigma^H$  is  $\sigma^f$  (friction corrected stress);  $T_0$  is target test temperature;  $T_i$  is the actual deformation temperature with  $T_i = T_0 + \Delta T$ .

Fig.14a and 14b show the true stress-strain curves before and after deformation heating correction at 250 °C and at strain rate of 0.1 s<sup>-1</sup>, respectively. It is apparent that the impact of temperature rise on the flow stress is more pronounced at higher strain rates and lower temperatures. And as the strain increases, the difference between the two curves is more significant. At 200 °C/1 s<sup>-1</sup>, the maximum temperature rise reaches 35 K and the flow stress reduction caused by temperature rise is 51 MPa.

## 2.4 Kinetic analysis

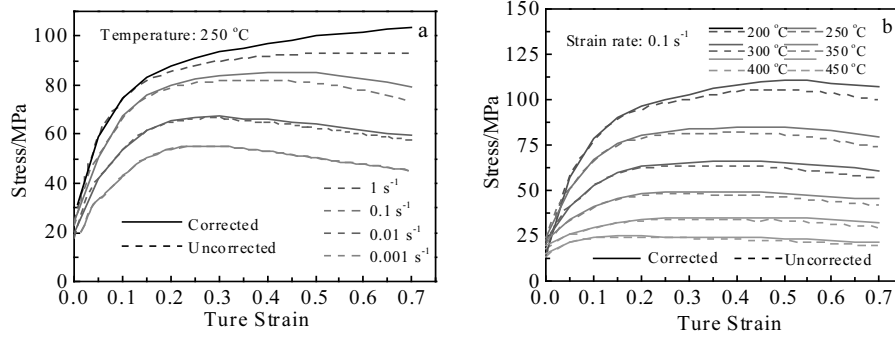


Fig.14 Comparison of the true stress-strain curves before and after deformation heating correction under different conditions: (a)  $T=250\text{ }^{\circ}\text{C}$  and (b)  $\dot{\epsilon}=0.1\text{ s}^{-1}$

### 2.4.1 Determination of material parameters

Malik et al.<sup>[34]</sup> proposed a widely accepted constitutive model to describe the relationship between the Zener-Hollomon parameter ( $Z$ )<sup>[19]</sup> and flow stress, deformation temperature and strain rate. It can be expressed as follows<sup>[35]</sup>:

$$Z = \dot{\epsilon} \exp\left(\frac{Q}{RT}\right) = \begin{cases} A_1 \sigma^{n_1} & \alpha\sigma < 0.8 \\ A_2 \exp(\beta\sigma) & \alpha\sigma > 1.2 \\ A[\sinh(\alpha\sigma)]^n & \text{for all } \sigma \end{cases} \quad (7)$$

where  $\sigma$  is the flow stress (MPa);  $\dot{\epsilon}$  is the strain rate ( $\text{s}^{-1}$ );  $A$ ,  $A_1$ ,  $A_2$ ,  $\beta$ ,  $\alpha$ ,  $n_1$  and  $n$  are material constants;  $Q$  is deformation activation energy ( $\text{kJ}\cdot\text{mol}^{-1}$ );  $R$  is the gas constant ( $8.314\text{ J}\cdot\text{mol}^{-1}\cdot\text{K}^{-1}$ );  $T$  is the absolute temperature (K). The relationship among  $\alpha$ ,  $\beta$  and  $n_1$  can be expressed as Eq.(8):

$$\alpha = \frac{\beta}{n_1} \quad (8)$$

From Eq.(7), different equations should be adopted to different stress levels. The power law is preferred at low stresses, and the exponential law is suitable at relatively high stresses. The hyperbolic sine law can be used for all stress ranges. Taking the natural logarithm on both sides of Eq.(7), and then Eq.(9) is obtained as follows:

$$\ln Z = \ln \dot{\epsilon} + \frac{Q}{RT} = \begin{cases} \ln A_1 + n_1 \ln \sigma & \alpha\sigma < 0.8 \\ \ln A_2 + \beta\sigma & \alpha\sigma > 1.2 \\ \ln A + n \ln[\sinh(\alpha\sigma)] & \text{for all } \sigma \end{cases} \quad (9)$$

Assuming that deformation activation energy  $Q$  is not a function of temperature  $T$ , according to Eq.(9), the values of  $n_1$ ,  $\beta$  and  $n$  can be defined as follows:

$$n_1 = \left[ \frac{\partial \ln \dot{\epsilon}}{\partial \ln \sigma} \right]_T \quad (10)$$

$$\beta = \left[ \frac{\partial \ln \dot{\epsilon}}{\partial \sigma} \right]_T \quad (11)$$

$$n = \left\{ \frac{\partial \ln \dot{\epsilon}}{\partial [\ln \sinh(\alpha\sigma)]} \right\}_T \quad (12)$$

If the strain rate  $\dot{\epsilon}$  is a constant,  $Q$  can be calculated by Eq.(13):

$$Q = R \cdot \left\{ \frac{\partial \ln \dot{\epsilon}}{\partial \ln[\sinh(\alpha\sigma)]} \right\}_T \cdot \left\{ \frac{\partial \ln[\sinh(\alpha\sigma)]}{\partial \left(\frac{1}{T}\right)} \right\}_{\dot{\epsilon}} = RnD \quad (13)$$

The discrete flow stress data at strains ranging from 0.05 to 0.7 with an interval of 0.05 are used to calculate the mentioned parameters. Fig.15a~15d show the relationships between  $\ln \dot{\epsilon}$  and  $\sigma$ ,  $\ln \dot{\epsilon}$  and  $\ln \sigma$ ,  $\ln \dot{\epsilon}$  and  $\ln[\sinh(\alpha\sigma)]$ ,  $\ln[\sinh(\alpha\sigma)]$  and  $1/T$ . According to Eqs.(10~12), the slopes of corresponding regression lines represent  $1/n_1$ ,  $1/\beta$ ,  $n$  and  $D$ , respectively. So the values of  $\alpha$ ,  $n$  and  $Q$  at strain of 0.6 can be calculated as 0.024, 5.84 and 148.90 kJ/mol according to Eq.(8) and Eq.(13).

The parameters  $A$  and  $n$  can be obtained from Eq.(14):

$$\ln Z = \ln A + n \ln[\sinh(\alpha\sigma)] \quad (14)$$

The relationship between  $\ln Z$  and  $\ln[\sinh(\alpha\sigma)]$  at strain of 0.6 is described in Fig.15e. The data are then fitted through linear regression, and the slope (5.88) and intercept (24.96) represent  $n$  and  $\ln A$  at strain of 0.6, respectively. The relative difference between the  $n$  values in Eq.(12) and Eq.(14) is less than 0.8%.

The evaluation of values for  $\alpha$ ,  $Q$ ,  $n$ , and  $\ln A$  at various strains with the range of 0.05~0.7 and the interval of 0.05 are calculated by the corresponding flow stress. Fig.16 displays the variations of  $\alpha$ ,  $Q$ ,  $n$ , and  $\ln A$  with strain, which can be described by the 6th-order polynomial relationships, as given in Eq.(15). The equation fitting coefficients of  $\alpha$ ,  $n$ ,  $\ln A$  and  $Q$  for Mg-3Sn-1Mn-1La alloy are given in Table 2.

$$\begin{cases} \alpha = B_1 + B_2 \epsilon + B_3 \epsilon^2 + B_4 \epsilon^3 + B_5 \epsilon^4 + B_6 \epsilon^5 + B_7 \epsilon^6 \\ n = C_1 + C_2 \epsilon + C_3 \epsilon^2 + C_4 \epsilon^3 + C_5 \epsilon^4 + C_6 \epsilon^5 + C_7 \epsilon^6 \\ \ln A = D_1 + D_2 \epsilon + D_3 \epsilon^2 + D_4 \epsilon^3 + D_5 \epsilon^4 + D_6 \epsilon^5 + D_7 \epsilon^6 \\ Q = E_1 + E_2 \epsilon + E_3 \epsilon^2 + E_4 \epsilon^3 + E_5 \epsilon^4 + E_6 \epsilon^5 + E_7 \epsilon^6 \end{cases} \quad (15)$$

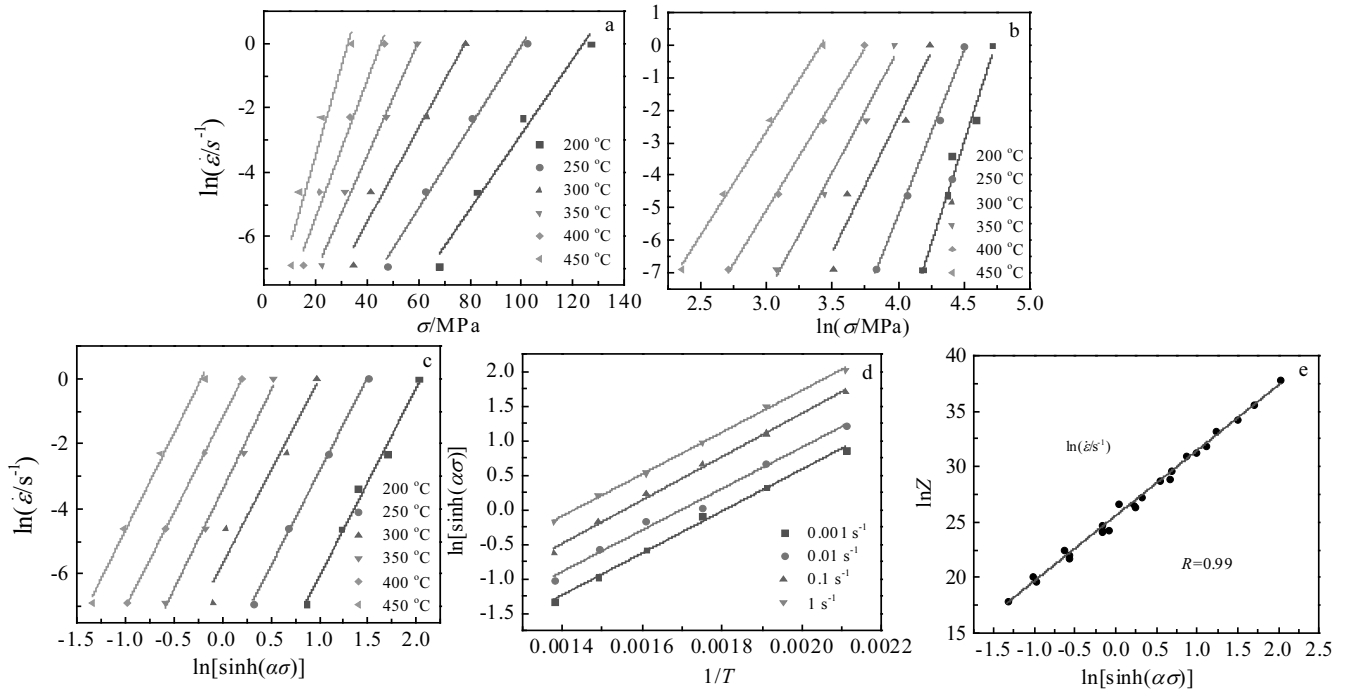


Fig.15 Relationship between  $\ln \dot{\epsilon}$  and  $\sigma$  (a),  $\ln \dot{\epsilon}$  and  $\ln \sigma$  (b),  $\ln \dot{\epsilon}$  and  $\ln[\sinh(\alpha\sigma)]$  (c),  $\ln[\sinh(\alpha\sigma)]$  and  $1/T$  (d), and  $\ln Z$  and  $\ln[\sinh(\alpha\sigma)]$  (e)

Table 2 Coefficients of polynomial functions

$\alpha$	$n$	$\ln A$	$Q/kJ \cdot mol^{-1}$
$B_1=0.03$	$C_1=8.51$	$D_1=15.04$	$E_1=101\ 715.11$
$B_2=-0.06$	$C_2=-42.60$	$D_2=137.81$	$E_2=622\ 409.50$
$B_3=-0.26$	$C_3=426.38$	$D_3=-303.37$	$E_3=-1.12 \times 10^6$
$B_4=2.64$	$C_4=-1\ 864.29$	$D_4=-588.67$	$E_4=-4.28 \times 10^6$
$B_5=-7.09$	$C_5=3\ 916.88$	$D_5=-2\ 938.67$	$E_5=1.75 \times 10^7$
$B_6=8.21$	$C_6=-3\ 962.90$	$D_6=-3\ 767.87$	$E_6=-2.22 \times 10^7$
$B_7=-3.54$	$C_7=1\ 556.78$	$D_7=1\ 622.66$	$E_7=9.64 \times 10^6$

Taking the inverse function of Eq.(7), the flow stress can be expressed as Eq.(16):

$$\sigma = \frac{1}{\alpha} \left\{ \left( \frac{Z}{A} \right)^{\frac{1}{n}} + \left[ \left( \frac{Z}{A} \right)^{\frac{2}{n}} + 1 \right]^{\frac{1}{2}} \right\} = \frac{1}{\alpha(\dot{\epsilon})} \ln \left\{ \left[ \frac{\dot{\epsilon} \exp\left(\frac{Q(\dot{\epsilon})}{RT}\right)}{A(\dot{\epsilon})} \right]^{\frac{1}{n(\dot{\epsilon})}} + \left[ \left( \frac{\dot{\epsilon} \exp\left(\frac{Q(\dot{\epsilon})}{RT}\right)}{A(\dot{\epsilon})} \right)^{\frac{2}{n(\dot{\epsilon})}} + 1 \right]^{\frac{1}{2}} \right\} \quad (16)$$

#### 2.4.2 Verification of the developed constitutive equations

In order to verify the accuracy of the developed constitutive equations, experimental results are compared with the calculated values for the entire range of strain, deformation temperature and strain rate, as shown in

Fig.17. It can be observed that the calculated flow stresses have the same trend with the experimental results. The calculated flow stress gives a good approximation to the experimental stress.

Besides the visual examination, the correlation coefficient ( $R$ ) and average absolute relative error (AARE) are used to further assess the credibility of the model, which can be expressed as Eq.(17) and Eq.(18), respectively:

$$R = \frac{\sum_{i=1}^N (X_i - \bar{X})(Y_i - \bar{Y})}{\sqrt{\sum_{i=1}^N (X_i - \bar{X})^2} \sqrt{\sum_{i=1}^N (Y_i - \bar{Y})^2}} \quad (17)$$

$$AARE = \frac{1}{N} \sum_{i=1}^N \left| \frac{X_i - Y_i}{X_i} \right| \times 100\% \quad (18)$$

where  $X_i$  and  $Y_i$  are experimental values and theoretical prediction values, respectively;  $\bar{X}$  and  $\bar{Y}$  are average experimental values and average theoretical prediction values, respectively;  $N$  is the number of data points used in the calculation.

As presented in Fig.18, a good correlation ( $R=0.984$ ) exists between the predicted and experimental stresses. The value of AARE is 4.426%. From the above analyses, it can be concluded that the strain-compensated constitutive equation can adequately describe the flow behavior of the Mg-3Sn-1Mn-1La alloy.

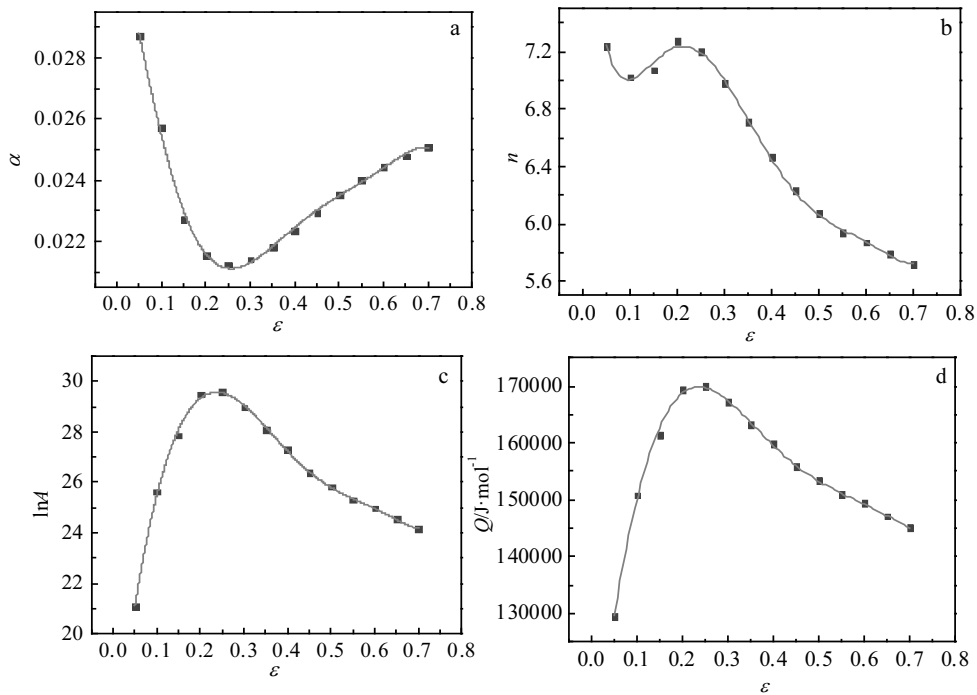


Fig.16 Relationships between constitutive constants and true strain: (a)  $\alpha$ - $\epsilon$ , (b)  $n$ - $\epsilon$ , (c)  $\ln A$ - $\epsilon$ , and (d)  $Q$ - $\epsilon$

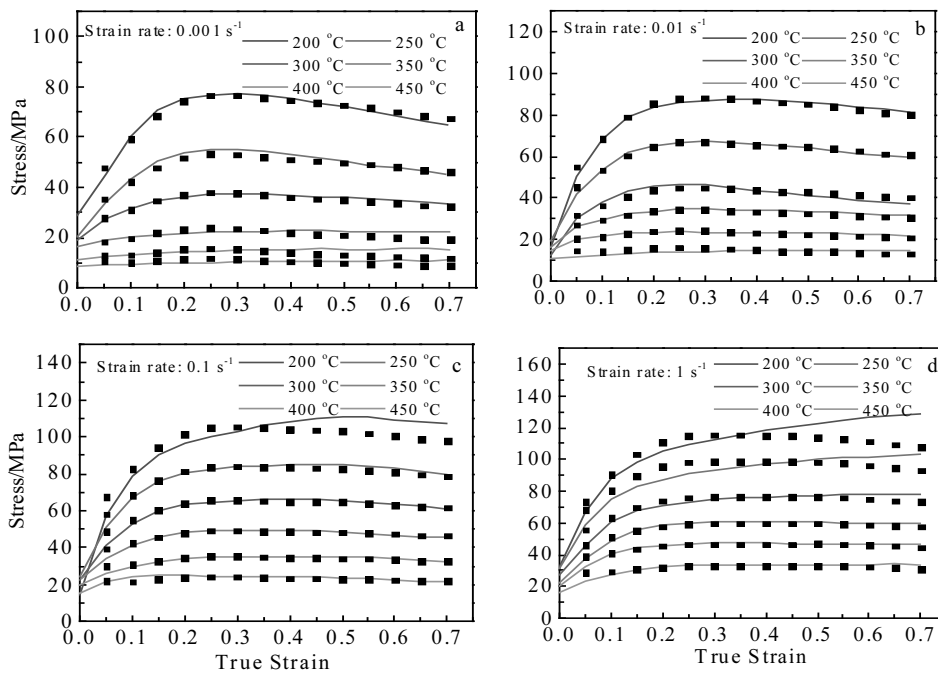


Fig.17 Relationships between calculated and experimental stress and true strain under different strain rates: (a)  $0.001 \text{ s}^{-1}$ , (b)  $0.01 \text{ s}^{-1}$ , (c)  $0.1 \text{ s}^{-1}$ , and (d)  $1 \text{ s}^{-1}$

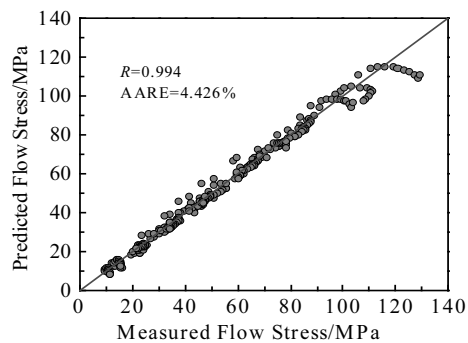


Fig.18 Correlation between calculated and experimental stresses

### 3 Conclusions

1) The flow stress increases rapidly and reaches a peak value in the early stage, and then gradually decreases until the steady state. The whole hot deformation process is mainly affected by the work hardening and dynamic softening effects.

2) According to microstructural evolution analysis, as the deformation temperature increases and the strain rate decreases, the dynamic recrystallization grain size increases during hot deformation. Continuous dynamic recrystallization mainly occurs at low deformation temperature and high strain rate, while the discontinuous dynamic recrystallization is the main dynamic recrystallization mechanism at high deformation temperature and low strain rate.

3) Plate-shaped MgSnLa compounds with the average length of 2  $\mu\text{m}$  and the average width of 250 nm are coherent with the  $\alpha\text{-Mg}$  matrix. Meanwhile, the spheroidized  $\text{Mg}_2\text{Sn}$  phases with the average diameter of 80 nm form in the  $\alpha\text{-Mg}$  matrix. These two types of precipitates effectively pin the movement of dislocation and improve the mechanical properties of the Mg-3Sn-1Mn-1La alloy.

4) Due to the application of suitable graphite sheet and lubricant, the frictional effect on the flow stress is slight. However, the deformation heating effect increases significantly with the decrease of the temperature and the increase of the strain rate. At 200  $^\circ\text{C}/1 \text{ s}^{-1}$ , the maximum temperature rise reaches 35 K and the maximum flow stress reduction caused by temperature rise is 51 MPa.

5) Based on the Arrhenius constitutive models, a strain-compensated constitutive equation is developed from the corrected friction and deformation heating stress-strain curves to predict the flow stress. The accuracy of the developed constitutive equations is assessed by statistical analyses, and the constitutive equations show highly precise prediction for the hot deformation flow stress of the Mg-3Sn-1Mn-1La alloy.

### References

- Ding Xiaofeng, Zhao Fuqiang, Shuang Yuanhua et al. *Journal of Materials Processing Tech*[J], 2020, 276: 116-125
- Zhao Zhanyong, Guan Renguo, Zhang Jianhong et al. *Acta Metallurgica Sinica*[J], 2017, 30(1): 66
- Poddar P, Sahoo K L. *Materials Science & Engineering A*[J], 2012, 556: 891
- Zhao Chaoyue, Chen Xianhua, Pan Fusheng et al. *Materials Science & Engineering A*[J], 2018, 713: 244
- Zhong Liping, Wang Yongjian, Dou Yuchen et al. *Journal of Magnesium and Alloys*[J], 2019, 7(4): 637
- Guan Renguo, Zhao Zhanyong, Chao Runze et al. *Transactions of Nonferrous Metals Society of China*[J], 2013, 23(1): 73
- Huang Xuefei, Huang Weigang. *Materials Characterization*[J], 2019, 151: 260
- Cong Wang, Yunteng Liu and Tao Lin et al. *Materials Characterization*[J], 2019, 157: 109-116
- Yang Mingbo, Pan Fusheng. *Materials Science & Engineering A*[J], 2009, 525(1): 112
- Zhang Min, Zhang Wenzheng, Zhu Guozhen et al. *Transactions of Nonferrous Metals Society of China*[J], 2007, 17(6): 1428
- Yang Mingbo, Qin Caiyuan, Pan Fusheng et al. *Transactions of Nonferrous Metals Society of China*[J], 2011, 21(10): 2168
- Wei Shanghai, Chen Yungui, Tang Yongbai et al. *Materials Science & Engineering A*[J], 2009, 508(1-2): 59
- Guan R G, Shen Y F, Zhao Z Y et al. *Scientific Reports*[J], 2016, 6: 23154
- Liu Shuhui, Pan Qinglin, Li Mengjia et al. *Materials & Design*[J], 2019, 184: 108-114
- Lin Y C, Chen X M. *Materials & Design*[J], 2011, 32(4): 1733
- Chen Gaojin, Chen Liang, Zhao Guoqun et al. *Journal of Alloys and Compounds*[J], 2017, 710: 80
- Gao L, Luo A A. *Materials Science & Engineering A*[J], 2013, 560: 492
- Cheng Weili, Bai Yang, Ma Shichao et al. *Journal of Materials Science & Technology*[J], 2019, 35(6): 1198
- Zhang Jingqi, Di Hongshuang, Wang Xiaoyu et al. *Materials & Design*[J], 2013, 44: 354
- Tahreen N, Zhang D F, Pan F S et al. *Materials & Design*[J], 2015, 87: 245
- Tahreen N, Zhang D F, Pan F S et al. *Journal of Alloys and Compounds*[J], 2015, 644: 814
- Liu G H, Li T R, Wang X Q et al. *Materials Science & Engineering A*[J], 2020, 773: 138-144
- Dai Q S, Deng Y L, Tang J G et al. *Transactions of Nonferrous Metals Society of China*[J], 2019, 29(11): 2252
- Wu H Y, Wu C T, Yang J C et al. *Materials Science & Engineering A*[J], 2014, 607: 261
- Su Zexing, Wan Li, Sun Chaoyang et al. *Materials Characterization*[J], 2016, 122: 90

- 26 Hao M J, Cheng W L, Wang L F et al. *Materials Science & Engineering A*[J], 2019, 748: 418
- 27 Ansari N, Tran B, Poole W J et al. *Materials Science & Engineering A*[J], 2020, 777: 139 051
- 28 Li Xinyu, Xia Weijun, Yan Hongge et al. *Materials Science & Engineering A*[J], 2019, 753: 59
- 29 Khorasani F, Emamy M, Malekan M et al. *Materials Characterization*[J], 2019, 147: 155
- 30 Tang Y, Le Q C, Jia W T et al. *Materials Science & Engineering A*[J], 2017, 704: 344
- 31 Tang C P, Wang X Z, Liu W H et al. *Materials Science & Engineering A*[J], 2019, 759: 172
- 32 Ebrahimi R, Najafizadeh A. *Journal of Materials Processing Tech*[J], 2004, 152: 136
- 33 Laasraoui A, Jonas J J. *Metallurgical Transactions A*[J], 1991, 22: 1545
- 34 Malik A, Wang Y W, Cheng H W et al. *Materials Science & Engineering A*[J], 2020, 771: 138 649
- 35 Hu Y L, Lin X, Li Y L et al. *Materials & Design*[J], 2020, 186: 108 359

## Mg-3Sn-1Mn-1La 镁合金热压缩组织演变与应变修正本构方程

张利斌<sup>1,3</sup>, 刘光明<sup>1,3</sup>, 韩廷状<sup>1,3</sup>, 黄闻战<sup>1</sup>, 王荣军<sup>2,3</sup>, 马立峰<sup>2,3</sup>

(1. 太原科技大学 材料科学与工程学院, 山西 太原 030024)

(2. 太原科技大学 机械工程学院, 山西 太原 030024)

(3. 太原科技大学 太原重型机械装备协同创新中心, 山西 太原 030024)

**摘要:** 通过对铸态 Mg-3Sn-1Mn-1La 合金在变形温度为 200~450 °C、应变速率为 0.001~1.0 s<sup>-1</sup> 条件下进行热压缩实验, 研究了其热变形行为和微观组织变化规律。结果表明: 随着变形温度的降低和应变速率的升高, 流变应力明显增大而再结晶晶粒尺寸减小。在变形温度较低条件下, 连续动态再结晶是主要的再结晶机制。然而, 当变形温度升高时, 非连续动态再结晶机制占主导。分析和修正了摩擦和变形热对流变应力的影响。结果表明, 与摩擦相比变形热对流变应力的影响更加明显, 且随着应变速率的增加和变形温度的降低, 变形热对流变应力的影响更加明显。在实验数据的基础上建立了应变修正的本构方程。通过对实验值与预测值的对比发现, 所建立的本构方程能够准确地描述实验合金的热变形行为。

**关键词:** Mg-Sn合金; 热压缩; 本构方程; 动态再结晶

作者简介: 张利斌, 男, 1992 年生, 硕士, 太原科技大学材料科学与工程学院, 山西 太原 030024, E-mail: 386066073@qq.com